Environmental Science Nano

Influence of Aluminum Incorporation and Aqueous Conditions on Metal Ion Release of High-Ni Transition Metal Oxide Nanomaterials

Journal:	*Environmental Science: Nano*
Manuscript ID	EN-ART-05-2023-000304.R1
Article Type:	Paper

Environmental Impact Statement

Understanding how technologically relevant metal oxides transform under environmentally and biologically relevant aqueous conditions is essential for assessing their potential environmental impacts. Al doping plays an important role in tuning the structural stability and performance of high-Ni cathode materials produced in high volumes for car batteries. We demonstrate how Al doping alters transformations of high-Ni nanomaterials under environmentally relevant aqueous conditions by comparing metal ion release for $LiNi_{0.80}Co_{0.20}O_2$ and $LiNi_{0.82}Co_{0.15}Al_{0.03}O_2$ nanomaterials. The experimental studies and modeling demonstrate how material properties can vary based on chemical constituents in the aqueous setting by comparing two aqueous media formulations. These results provide important new fundamental insights into the factors that control potential release and environmental impact of this industrially important class of nanomaterials.

Influence of Aluminum Incorporation and Aqueous Conditions on Metal Ion Release of High-Ni Transition Metal Oxide Nanomaterials

Blake G. Hudson[a], Curtis M. Green[b], Arun Kumar Pandiakumar[b], Ali Abbaspour Tamijani[a], Natalie V. Hudson-Smith[c], Joseph T. Buchman[c], Meagan Koss[d], Elizabeth D. Laudadio[b], Michael P. Schwartz[b], Rebecca Klaper[d], Christy L. Haynes[b], and Robert J. Hamers[b], and Sara E. Mason[a,e,*]

[a] *Department of Chemistry, University of Iowa, Iowa City, IA 52242, USA.*

[b] *Department of Chemistry, University of Wisconsin-Madison, Madison, WI 53706, USA*

[c] *Department of Chemistry, University of Minnesota, Minneapolis, MN 55455, USA.*

[d] *School of Freshwater Sciences, University of Wisconsin-Milwaukee, Milwaukee, WI 53204, USA.*

[e] *Center for Functional Nanomaterials, Brookhaven National Laboratory, Upton, NY 11973, USA.*

ABSTRACT

Developing a materials perspective of how to control the degradation and negative impact of complex metal oxides requires an integrated understanding of how these nanomaterials transform in the environment and interact with biological systems. Doping with aluminum is known to stabilize oxide surfaces, but has not been assessed cohesively from synthesis to environmental fate and biological impact. In the present study, the influence of aluminum on metal ion release from transition metal oxides was investigated by comparing aqueous transformations of lithium nickel cobalt aluminum oxide ($LiNi_{0.82}Co_{0.15}Al_{0.03}O_2$; NCA) and lithium nickel cobalt oxide ($LiNi_{0.80}Co_{0.20}O_2$; NC) nanoparticles and by calculating the energetics of metal release using a density functional theory (DFT) and thermodynamics method. Two model environmental organisms were used to assess biological impact, and metal ion release was compared for NCA and NC nanoparticles incubated in their respective growth media; moderately hard reconstituted water (MHRW) for the freshwater invertebrate *Daphnia magna* (*D. magna*) and minimal growth medium for the Gram-negative bacterium *Shewanella oneidensis*-MR1 (*S. oneidensis*). The amount of metal ions released was reduced for NCA compared to NC in MHRW, which correlated to changes in the energetics of release upon Al substitution in the lattice determined by DFT and thermodynamics modeling. In minimal medium, metal ion release was approximately an order of magnitude higher compared to MHRW and was similar to the stoichiometry of the bulk nanoparticles for both NCA and NC. Computational modeling demonstrated that the increase in total metal ion release and the reduced influence of Al doping arises from lactate complexation of metal ions in solution. The relative biological impacts of NC and NCA exposure for both *S. oneidensis* and *D. magna* were consistent with the metal release trends observed for minimal medium and MHRW, respectively. Together, these results demonstrate how a combined experimental and computational approach provides valuable insight into the aqueous transformations and biological impacts of complex metal oxide nanoparticles.

1. Introduction

Chemical reactivity of oxide surfaces has widespread environmental impacts, such as by altering the composition of natural waters, contaminant fate and transport, the formation of atmospheric aerosols, microbially-mediated redox processes, geologic CO_2 sequestration, and environmental catalysis.[1-6] Recent increases in the widespread use of anthropogenic nanoparticles, particularly nanoparticles containing elements with significant toxicity in the environment, has placed increased emphasis on a need to understand the fundamental chemical transformations of nanomaterials with complex compositions (e.g., containing multiple transition metals) and in media representative of natural environments.[7-9] Microparticles and nanoparticles based on $LiCoO_2$ and related compositions with the delafossite crystal structure represent a particularly important family of complex metal oxides (CMOs) due to their widespread use as the active cathode material in lithium ion batteries (LIBs).[10-15] The high cost and limited worldwide supply of Co has fostered great interest in replacing $LiCoO_2$ with alternative compositions that achieve good performance using more earth-abundant elements, Ni and Al.[16-18] This has led to development of complex metal oxides with compositions such as $LiNi_xMn_yCo_{1-x-y}O_2$ (NMC) and $LiNi_xCo_yAl_{1-x-y}$ (NCA), which now form the basis of the batteries used in the majority of electric vehicles worldwide.[19-24] The absence of globally mandated pathways for recycling of battery cathode materials has led to increasing concerns about the potential environmental impacts associated with end-of-life disposal.[25]

The confluence of high demand of LIBs and lack of recycling options gives growing concern to the exposure of nanoscale CMOs to environmental settings. Experiments done under simulated landfill conditions show that disposed LIBs can leach out toxic metals such as Co and Ni.[26] The biological impacts of CMO exposure to aqueous conditions can be understood, in part, through studies of how the nanomaterials transform in those settings. For example, in a study of *Shewanella oneidensis* MR-1 exposure to $Li(Ni_{.33}Mn_{.33}Co_{.33})O_2$ ("333-NMC") in bacterial medium, it was determined that release of constituent metals (especially aqueous Ni^{2+} and Co^{2+}) was the primary source of toxicity.[27] It was observed that while the initial NMC composition had equal amounts of Ni, Mn, and Co, the metals were not released at similar amounts; instead, the measured release follow the trend of Ni > Co > Mn (an "incongruent" metal release trend). Over

time, the metal release resulted in a Ni- and Co-depleted nanomaterial with altered composition and structure. In a subsequent study, modeling using a combined density functional theory (DFT) and thermodynamics methodology was shown to capture the trend in incongruent metal release.[28]

The conclusion that toxicity of NMC nanomaterials towards *S. oneidensis* arises from aqueous cations formed from the constituent transition metals motivated a body of work aimed at understanding the relationship between the solid-state stoichiometry and trends in the relative amounts of metals released. Here, we refer to "metal release" to disambiguate from "dissolution," as the dissolution of layered lithium intercalation materials, which goes on to include delithiation steps and structural evolution of the oxide.[29-31] Compositional tuning, or variation of the relative amounts of metals within a bulk CMO material, provides a route to designing cathode materials with tailored release properties. This strategy could be used to intentionally reduce the release of toxic transition metals or promote release for easier recycling methods. For example, in Ni-enriched NMC, such as $LiNi_{0.6}Mn_{0.2}Co_{0.2}O_2$ (622-NMC), Ni is released at higher concentrations than 333-NMC due to the change in metal ratios, but at lower concentrations than expected based on the percent change in the bulk material. DFT modeling was used to show that Ni-enriched NMC leads to a higher fraction of Ni present in more stable 3+ and 4+ oxidation states, providing a chemical explanation for the release trend.[32] Other studies varying the NMC composition, with accompanying biological studies and computational modeling, confirmed roles for metal release in NMC toxicity towards *S. oneidensis* and the relationship between changes in bulk oxidation states and metal release.[33, 34]

Doping, or the intentional addition of a relatively small amount of an impurity to a material, is another means of tuning material properties. The incorporation of small amounts (~5%) of aluminum into NC ($LiNi_{0.80}Co_{0.20}O_2$), to form NCA ($LiNi_xCo_yAl_{1-x-y}O_2$), has been shown to improve the chemical stability and reduce the release of transition metals into the non-aqueous solvents used in batteries.[35] However, the influence of Al on the corresponding aqueous-phase chemistry that largely control the environmental impacts of improper disposal has not been explored.

In the present study we aim to understand how doping with aluminum influences metal release for high-Ni layered metal oxides by comparing nanoscale NC ($LiNi_{0.80}Co_{0.20}O_2$) and aluminum-doped materials, referred to as NCA, using experimental measurements and computational methods. In NCA compositions, the Ni, Co, and Al are all initially present in the 3+ oxidation state. Therefore, any composition-dependent changes in metal release must be linked to other factors, such as the thermodynamic stability of Al inclusion. Because the composition of the aqueous medium can also play an important role in the overall chemistry, we investigated how aqueous conditions affect metal release from NCA and NC by comparing two common media formulations used to grow freshwater organisms: moderately hard reconstituted water ("MHRW", *D. magna* growth medium) and minimal medium (*S. oneidensis* growth medium). The primary differentiating factor between the two media is the presence of lactate in minimal medium, a known chelating agent that stabilizes released metals in solution.

Our results show that metal ion release is substantially higher in minimal medium than in MHRW for NC and NCA, which is consistent with prior results from the NMC family in these same media.[27, 32, 36] Our comparison of metal release for NC vs. NCA shows that incorporation of Al significantly reduces metal ion release in MHRW, with a preferential release of Ni (incongruent release), but in minimal medium, transition metal release is similar to the mole fraction composition in the bulk nanomaterial (congruent release). Using a computational approach that links density functional theory (DFT) with thermodynamically accessible energies, we provide insight into the mechanisms of aqueous metal ion release for NC and NCA, including the role of lactate, changing metal release profiles. Additionally, we demonstrate that biological impacts for two model organisms exposed to NC and NCA nanoparticles are consistent with experimental and computational metal release trends. The ability to link material properties to dissolution trends and subsequent biological impact has broader implications for a wide range of technologically relevant nanotechnologies.

2. Experimental

2.1 Molten salt synthesis of $LiNi_{0.82}Co_{0.15}Al_{0.03}O_2$ (NCA)

We first synthesized $LiNi_{0.82}Co_{0.15}Al_{0.03}(OH)_2$ (NCA hydroxide) using a co-precipitation reaction of metal salts in the presence of a chelator following methods that have been shown to form materials with a homogeneous distribution of constituent elements.[37-41] To form NCA hydroxide, an aqueous solution containing 0.15 M nickel(II) sulfate hexahydrate ($NiSO_4.6H_2O$), 0.028 M cobalt(II) sulfate heptahydrate ($CoSO_4.7H_2O$), 0.0047 M aluminum(III) sulfate hexadecahydrate ($Al_2(SO_4)_3.16H_2O$), and 0.5 M 5-sulfosalicylic acid was prepared. The metal salt solution was then transferred to a burette and added quickly to a beaker containing a stirring aqueous solution of 4 M lithium hydroxide to promote co-precipitation of NCA hydroxide. The chelating agent 5-sulfosalicylic acid limits the concentration of free metal ions and thereby reduces overall supersaturation for formation of metal hydroxides (pH ~12-13).[40] After addition of the chelated metal salts to the LiOH solution, the resulting reaction mixture was stirred at room temperature for 30 minutes. The precipitate was then centrifuged at 4696 xg and washed with water three times to remove the excess ligand and residual ions. Finally, the NCA hydroxide precipitate was dried, yielding a green solid. Powder x-ray diffraction (PXRD) exhibited broad peaks (**Figure S1**) that are consistent with the formation of nanoscale NCA hydroxide particles.[42] A molten salt mixture was prepared using a 6:4 molar ratio of lithium nitrate and lithium hydroxide. The NCA hydroxide precursor was added to the molten salt mixture at 450°C and allowed to react for 30 minutes. The reaction mixture was quenched with water and the precipitate was washed with water three times and dried to obtain $LiNi_{0.82}Co_{0.15}Al_{0.03}O_2$ (NCA) nanoparticles.

2.2 Molten Salt Synthesis of $LiNi_{0.80}Co_{0.20}O_2$ (NC)

The $Ni_{0.80}Co_{0.20}(OH)_2$ (NC hydroxide) precursor was synthesized by adding an aqueous solution of 0.15 M nickel and 0.037 M cobalt sulfate salts to a lithium hydroxide solution. The NC hydroxide precursor was synthesized without 5-sulfosalicylic acid as a chelating agent as $Ni(OH)_2$ and $Co(OH)_2$ have similar K_{sp} and so are likely to co-precipitate homogeneously. The aqueous solutions of $NiSO_4.6H_2O$ and $CoSO_4.7H_2O$ were prepared and transferred to a burette and then added quickly to a stirring aqueous solution of 4 M lithium hydroxide, and then stirred at room temperature for 30 minutes. The resulting precipitate was centrifuged and washed with water three times and dried, yielding NC hydroxide as a green powder. The NC hydroxide precursor was added to a molten salt mixture (prepared by adding 6:4 molar ratio of lithium nitrate and lithium

hydroxide) at 450°C for 30 minutes. The reaction mixtures were quenched with water and then the precipitates were washed three times with water and dried in a vacuum oven to yield NC nanoparticles. See results and discussion for characterization of NC nanoparticles synthesized by the molten salt method.

2.3 Nanoparticle characterization

Scanning Electron Microscopy (SEM). SEM images were obtained using a Leo Supra55 VP scanning electron microscope. To obtain SEM images, dilute methanolic solutions of nanoscale NCA or NC were drop cast onto a boron-doped silicon wafer. SEM images were taken using both in-lens and SE2 detectors using incident beam acceleration voltages of 1 kV and 3 kV respectively.

Powder X-ray Diffraction. Powder XRD patterns were obtained using a Bruker D8 Advance Powder X-ray Diffractometer with Cu K_α radiation. NCA or NC powders were lightly pressed into the well of a zero-background SiO_2 plate from MTI Corp (Richmond, CA). XRD patterns were collected for diffraction angles 2θ in the range of 10-90˚ at a resolution of 0.1˚.

ICP-OES for nanoparticle composition. The composition of NCA and NC nanoparticles was determined by digesting samples in freshly prepared aqua regia (3:1 volume mixture of 37% HCl and 70% HNO_3) [**CAUTION: Aqua Regia is highly corrosive and may result in skin burns or explosion if not treated with extreme care!**]. The digested sample was then diluted with water and analyzed by ICP-OES. Concentration of metal ions was obtained as four analytical replicates employing an Agilent 5110 ICP-OES. Analysis of our calibration curves yielded detection limits of 0.3 μM for Ni, 0.15 μM for Co, 0.4 μM for Al, and 0.5 μM for Li. These detection limits are all well below the concentrations observed in the present studies.

ICP-OES for metal ion release. To determine the concentration of metal species released into the media, nanoparticle suspensions were stirred in either moderately hard reconstituted water (MHRW) at 20°C or in minimal medium at 30°C for 72 hours, with aliquots collected at 1, 3, 6, 24, 48, and 72 hours. The aliquots were centrifuged at 4696 x g for 30 minutes. The supernatant was then removed and acidified to achieve 2.5% by weight HNO_3, thereby matching the acid concentration of the standards used. The concentration of metal species was determined using two sample replicates and four analytical replicates by ICP-OES.

X-ray photoelectron spectroscopy. XPS analysis was used to measure the fractional composition of metal species present near the surface for NC and NCA nanoparticles before and after 72 hours incubation in moderately hard reconstituted water (MHRW **Figure S2**) and minimal medium (**Figure S3**). NCA and NC nanoparticles incubated in MHRW and in minimal medium were washed with water three times. Samples collected before and after incubation were then pressed into foil. XPS measurements were carried out on a PHI 5000 VersaProbe III using an Al K_α X-ray source at 45˚ takeoff angle and charge compensation via dual electron flood gun and ion gun. Survey spectra were recorded with a pass energy of 50 eV. CasaXPS software was used to determine the peak area for metal species in NCA and NC. The fractional composition for metal species at the surface of NC and NCA nanoparticles was determined using the following equation:

Eq 1. $$f_x = \frac{\frac{A_x}{S_x \lambda_x}}{\sum_i \frac{A_i}{S_i \lambda_i}}$$

Where x = Ni, Co or Al, A_i = area obtained from XPS for element i, S_i = atomic sensitivity factor for element i, and λ_i = inelastic mean free path for element i. Inelastic mean free path values of 2.07 nm (Ni), 2.24 nm (Co) and 3.78 nm (Al) were obtained using the NIST electron inelastic mean free path database[43] via the TPP-2M equation.[44]

2.4 Computational Modeling

Periodic calculations. Spin polarized DFT calculations were carried out on models of NC and NCA. Based on our previous benchmarking of different exchange-correlation functionals,[28] work here is done using the GGA-PBE exchange-correlation functional,[45] as implemented in the Quantum Espresso (QE) open source suite.[46, 47] GBRV ultrasoft pseudopotentials[48] were used to model electron-nucleus interactions. A planewave cutoff of 40 Ry was chosen for the wavefunction and a charge density threshold of 320 Ry was used, as recommended for the pseudopotential set.

Theoretical lattice constants were determined starting from the bulk structure of $LiNiO_2$ (LNO) based on an experimental crystallographic information file as reported in the Inorganic Crystal Structure Database.[49] Variable volume bulk cell geometry optimizations were run using a converged 8×8×4 Monkhorst-Pack[50] grid of *k*-points and imposing no constraints on atomic positions. A residual force criterion of 5 meV/Å was used. This material has an $R\bar{3}m$ symmetry (space group no. 166) and belongs to the delafossite structure type. The experimental (theoretical) lattice parameters for this structure are a = 2.883 (2.885) Å and c = 14.199 (14.113) Å.[51] The better agreement between theory and experiment for the in-plane lattice constant is

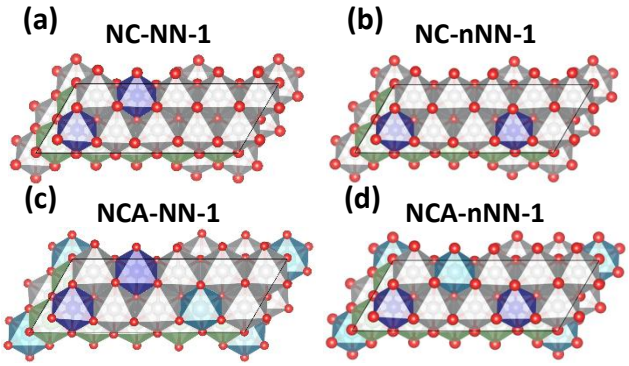

Figure 1: Skewed top-down view of structural figures for NC and NCA compositions with Ni (grey), Co (purple), and Al (blue). (a) and (b) show nearest neighbor (NN) and next-nearest neighbor (nNN) arrangements of Co in NC. (c) and (d) show the structural models with Al added to the lattice. Additional configurations were also tested to provide more varieties of chemical environments (**Figure S4**).

consistent with other results in the literature and is to be expected for the layered structure.[11, 52]

To generate NC and NCA surface models, we use the optimized bulk LNO as the parent structure to set up a 5×2 supercell as shown in Figure 1. From this surface we can substitute Co and Al in place of Ni to obtain the compositions $LiNi_{0.80}Co_{0.20}$ for NC and $LiNi_{0.70}Co_{0.20}Al_{0.10}O_2$ for NCA, additional structures are presented in the SI (**Figure S4**). These cells have three O-M-O tri-layers and are exposed to the vacuum region along the (001) direction. A comparison of NC vs NCA layer spaings is tabulated in the SI (**Table S1**), indicating non significant structural changes between the compositionally tuned surface models. All of these structural models have 10 metal ion sites per metal layer, which allows for various arrangements of neighboring environments for these compositions. We have assembled several structures labeled as nearest neighbor (NN, Figure 1 a and c), where Co atoms occupy edge-sharing sites in the surface plane, and next

nearest neighbor (nNN, Figure 1 b and d), where the two Co atoms are separated in the surface plane by a Ni atom.

In going from the bulk to surface supercell geometry, the k-point mesh was appropriately reduced to 2×4×1. A 20 Å thick vacuum was included along the surface normal direction to avoid spurious interactions between consecutive periodic images. Vibrational modes were computed using a frozen-phonon approach as implemented in Phonopy software[53] using a displacement of 0.01 Å.

The change in free energy associated with cation release was modeled by combining DFT calculations with accessible experimental solvation energy data. This DFT + Solvent Ion model[54] has been used in related work and the details of the approach used here are identical.[28, 32, 33, 52, 55-57] Relevant equations and model values are presented in **Equations S1-S7**. In brief, using the DFT + Solvent Ion model, metal release is modeled as the removal of an M-OH group (where M=Co, Al, or Ni). The process is divided into two steps: In the first step, the vacancy energy, referred to as ΔG_1, is calculated using DFT by comparing the total energy of the slab missing the M-OH group relative to the starting slab and M-OH constituents in their respective standard states. DFT total energies are related to Gibbs free energies by adding zero-point energy corrections and vibrational contributions for temperature effects. The redox and hydration of the leaving M-OH constituents are taken into account through terms referred to ΔG_2 (based on tabulated data for ΔG^0_{SHE}, see **Table S2**). In this way, solvation effects of the standard state species to its aqueous ions are taken into account. The free energy change for the overall Ni-OH removal denoted as ΔG_T, is given as a sum of ΔG_1 and ΔG_2 terms:

Eq 2 $$\Delta G_T = \Delta G_1 + \Delta G_2 = G[(\mathrm{LiMO_2})_{\mathrm{Ni-OH}\,(s)}] + G(\mathrm{H^+_{(aq)}}) \rightarrow G[(\mathrm{LiMO_2})_{\_(s)}] + G(\mathrm{Ni^{2+}_{(aq)}}) + G(\mathrm{H_2O_{(l)}}) + e^-$$

Here, $(\mathrm{LiMO_2})_{\text{Ni-OH}}$ represents a pristine surface with an intact Ni-OH group and $(\mathrm{LiMO_2})\_\_$ represents the surface after the Ni-OH is removed.

Each of the 5x2 surface supercell models allow consideration of distinct ways to remove the M-OH groups for a given metal. When comparing ΔG_T between NC and NCA removals, it is useful to consider removal schemes that have similar chemical environments in both compositions, as displayed in Figure 2.

Figure 2 shows top-views of the NC-NN Ni (a) and NCA-NN Ni (b) surfaces and defines the notation

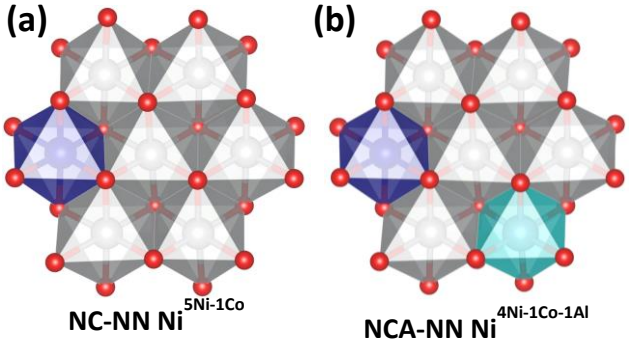

Figure 2: Top view of the local environment surrounding defect sites. Ni (grey), Co (purple), and Al (blue). Here, the site of the metal to be removed is in the center and is surrounding by six other metal sites. (a) starts from the NC-NN-1 slab (Fig. 1 (a)) and removes an Ni from the center. 5 of the surrounding metals are Ni and one is Co, so this structure is labeled NC-NN-1 $Ni^{5Ni\text{-}1Co}$. (b) starts from NCA-NN-1 (Fig. 1 (c)) and removes an Ni from the center. The resulting structure has an Ni vacancy surrounded by 4 Ni, 1 Co, and 1 Al, and is labeled NCA-NN-1 $Ni^{4Ni\text{-}1Co\text{-}1Al}$.

used for the vacancy structures formed by M-OH removals. When an Ni-OH group based on the central Ni atom in Figure 2(a) is removed, the resulting metal vacancy that is formed is surrounded by 5 Ni atoms and 1 Co. The resulting vacancy structure is denoted as NC-NN $Ni^{5Ni\text{-}1Co}$. By analogy, starting from the NCA-NN Ni surface in Figure 2(b) and removing an Ni-OH group based on the central Ni atom results in a vacancy structure denoted as NCA-NN $Ni^{4Ni\text{-}1Co\text{-}1Al}$.

A metric that has shown to be tied to trends in ΔG_T is the total spin of the metals directly coordinated to the vacancy site, which we denote as μ_B.[55] This value is taken as the summation of the magnetic moments in Bohr magneton of the six edge sharing metals as shown in Equation 3.

Eq 3. $$\mu_B = \sum_{i=1}^{6} \mu_{B,i}$$

In an effort to further relate the DFT calculations to known material functionality and observable properties, we model the thermodynamics of release of Li^+,[57] examining the fully (de)lithated structures. In turn, the change in energy associated with Li^+ release can be related to the intercalation voltage V_{int}. The calculation of V_{int} follows after previous computational studies [57, 58]:

Eq 4. $$V_{int} = \frac{E[Li_{0.00}MO_2] + E(Li_{metal}) \times (Li_{1.00} - Li_{0.00}) - E[Li_{1.00}MO_2]}{-(Li_{1.00} - Li_{0.00}) \times F}$$

Finally, As aluminum doping is expected to stabilize the lattice, we go on to calculate DFT formation enthalpies, using a Hess's law approach to products minus reactants.[55]

Molecular calculations. As reported previously, additional terms can be added to the DFT + Solvent Ion model to go on to consider subsequent aqueous chemistry between the hydrated cations formed from release and other species in solution.[32, 56] Specifically, here we consider steps in which aqueous cations of Ni, Co, and Al go on to form bi-lactated complexes, following after previous work.[32] To summarize, Pourbaix diagrams show Ni and Co both exist in a +2 oxidation state at pH 7.[59] The energy change associated with the bi-lactate ligand exchange reaction is deonted by , ΔG_3 , and are given in Table 1. The model reactions used for these energy changes are given in **Equations S3-S5**.

Table 1: ΔG_3 values for bi-lactate ligand exchange (**Equations S6 & S7**) for Ni[a], Co[a] and Al.

(eV)	**Co^{2+}**	**Ni^{2+}**	**Al^{3+}**
$\Delta \boldsymbol{G_3}$	-1.37[a]	-0.96[a]	-2.13

[a] Values taken from previous work.[32]

The values of ΔG_3 given in Table 1 are used to calculate $\Delta G_T^{'}$ as $\Delta G_T^{'} = \Delta G_T + \Delta G_3$ (**Tables S3-S5**). That is, values of $\Delta G_T^{'}$ represent the change in energy for the release of a Co-OH (or Ni-OH) group and subsequent formation of the corresponding bi-lactate complex, depicted in **Figure S5**.

2.5 Evaluation of biological impact

Biological impact was evaluated using two common organisms for environmental toxicology research: *Daphnia magna* (*D. magna*), which is found in freshwater aquatic environments, and *Shewanella oneidensis MR-1* (*S. oneidensis*), which is a ubiquitous soil bacterium.

***Daphnia magna* (*D. magna*).** *Daphnia magna* were harvested from cultures maintained in the Klaper lab at the UW-Milwaukee School of Freshwater Sciences. Daphnids were grown in MHRW incubated at 20°C on a 16:8 hour light/dark cycle according to EPA recommendations.[60] Daphnids were fed using a combination of 25 mL of freshwater algae (*Pseudokirchneriella subcapitata*) at an algal density of ~400,000 algal cells per mL and 10 mL of alfalfa supernatant

(*Medicago sativa*) three times weekly. Alfalfa supernatant was prepared by suspending 8,100 mg of alfalfa in 1 L of ultrapure Type 1 water, followed by 20 minutes of agitation at 130 RPM and 24 hours of sedimentation. Breeding populations were maintained at a population density of 20 adult daphnids per liter of daphnid media, kept in 1-L glass beakers. Neonates were harvested from daphnid adults between 14 and 28 days old, ensuring healthy neonates for use in exposures.

***D. magna* exposures.** Acute toxicity was measured for *D. magna* exposed to NCA or NC nanoparticles following a protocol similar to that used previously in studies of other complex transition metal oxide nanomaterials.[36] Briefly, acute exposures followed a modified protocol based on OECD 202 guidelines for the *D. magna* acute immobilization test.[27, 34, 61, 62] Five daphnid neonates (≤ 24 hours old) were placed in 30-mL glass beakers containing 10 mL of a given treatment. Four replicates were conducted for each treatment and the fraction of surviving animals was quantified visually after 48 hours without feeding. NC and NCA nanoparticles were tested at concentrations of 0 (control), 1, 10, 50, and 100 mg/L. NC and NCA stock suspensions were prepared by measuring out and mixing materials with ultrapure Type 1 water in a 250-mL glass vessel to a concentration of 1g/L. To create the desired exposure concentrations, the 1 g/L nanoparticle stock solution in ultrapure water was diluted with MHRW to bring the total volume to 10 mL at each given concentration. Stocks were then sonicated for 10 minutes immediately prior to addition to daphnid replicates.

Statistical analysis of *D. magna* survival data. In order to determine the significance of impacts of the NC and NCA treatments towards *D. magna* compared to controls, two statistical analyses, the nonparametric Tukey test and Kruskal-Wallis One Way ANOVA on Ranks tests, were chosen due to the distribution of data and the homogeneity of variances. The statistical analyses were performed using SigmaStat (Systat Software, San Jose, CA). Impacts of NC and NCA to daphnid survival were assessed using the nonparametric Tukey test since the data did not follow a normal distribution as determined by Shapiro Wilk normality tests.

***Shewanella oneidensis* MR-1 (*S. oneidensis*) culture and exposure.** *S. oneidensis* was cultured in minimal growth medium ("minimal medium" - 11.6 mM NaCl, 4.0 mM KCl, 1.4 mM $MgCl_2$, 2.8 mM Na_2SO_4, 2.8 mM NH_4Cl, 88.1 µM Na_2HPO_4, 50.5 µM $CaCl_2$, 10 mM HEPES, and 100 mM sodium lactate) for this study. The impact of NCA and NC nanoparticles on *S. oneidensis*

viability was tested using a growth based viability (GBV) assay as previously described.[63] Briefly, a working solution 10x more concentrated than target doses was prepared by suspending NCA into deionized water. This suspension is sonicated by bath sonication for 10 minutes and then diluted 1:1 to build a series of 10x concentrated working solutions. These suspensions are added to a bacterial suspension in minimal growth medium (OD_{600} = 0.1) in a 1:10 dilution such that desired doses (100, 50, 25, 12.5, 6.25 ppm) are achieved. A calibration curve of *S. oneidensis* MR-1 is also prepared by 1:1 dilution to create a series of S. oneidensis MR-1 suspensions, as described in the previous publication.[63] *S. oneidensis* MR-1 was exposed to NCA materials in minimal growth media for three hours. After three hours, 5 µL aliquots of these cultures were transferred to 195 µL of nutrient rich LB broth and allowed to grow up in a plate reader at 30°C overnight. OD_{600} was measured at 20 minute intervals. Growth curves were analyzed in R as described in Qiu et al.[63]

3. Results and Discussion

3.1 Synthesis of NC and NCA by molten salt method.

Nanoscale NCA and NC were synthesized by a molten salt method that has previously been used to produce high-purity single-phase materials.[64-67] For this method, the molten salt acts as a solvent that facilitates diffusion of reactants, which enables the synthesis of high purity materials at lower temperatures and shorter reaction times than those used in traditional calcination processes. Figure 3 shows XRD patterns (Figure 3a) and SEM images (Figure 3b) for NCA. The diffraction patterns in Figure 3a are similar to those reported previously for NC and NCA.[39] While the positions of the peaks are dependent primarily on the crystal structure (here, the delafossite structure), the detailed position and width of the individual diffraction peaks depends on the precise chemical composition, with additional broadening dependent on possible structural disorder and size-dependent broadening. In the XRD data, the intensity of the (003) peak relative to the (104) is a measure of structural disorder; the low intensity of the (003) peak indicates significant disorder in the lattice due to the differing spatial distribution of the metal cations, along with additional broadening due to the small nanoparticle size. We also performed transmission electron microscopy (TEM) of the nanoparticles, with **Figure S6** illustrating histograms of the longest dimension for each nanoparticle. SEM and TEM data each show that NC and NCA are similar in size, with a median length of approximately 25 nanometers.

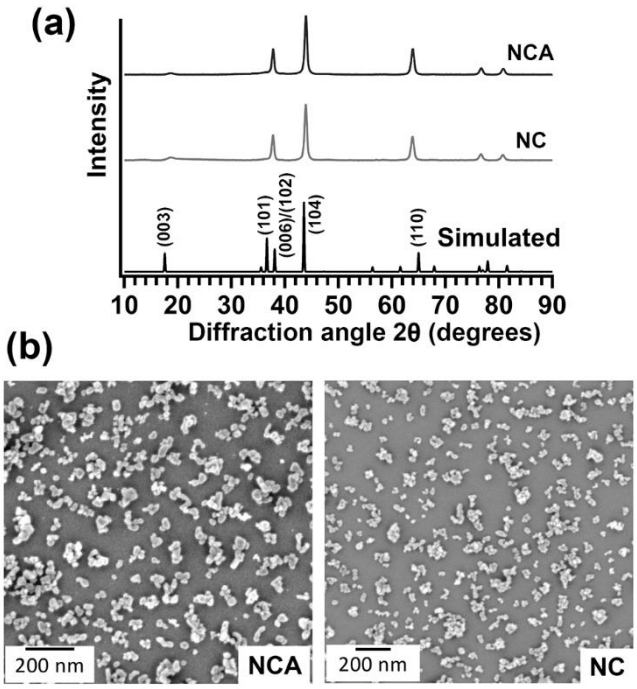

Figure 3. (a) X-ray diffraction patterns of NC and NCA and a simulated pattern for $LiNi_{0.80}Co_{0.20}O_2$. (b) Scanning electron micrographs of NCA (left) and NCA (right). Aggregation is observed in SEM is attributed to the effects of surface tension during drying of the samples.

3.2 Aqueous metal ion release for NCA and NC nanoparticles

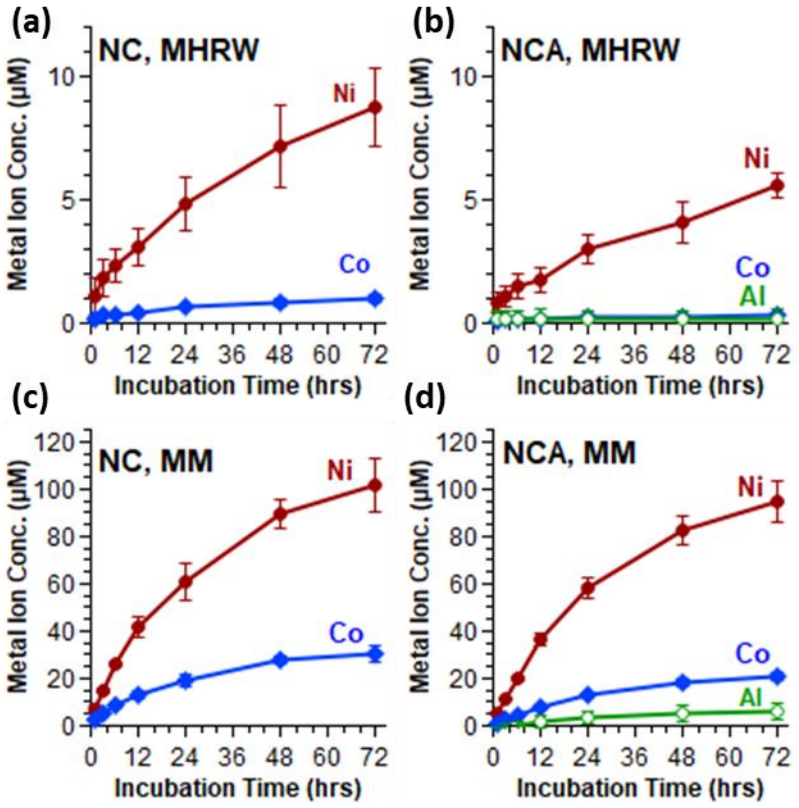

Figure 4. Aqueous metal ion dissolution for NCA and NC in minimal medium (MM) and moderately hard reconstituteded water (MHRW)
(a-b) Concentration of dissolved metal ion species released by 50 mg/L (a) NC and (b) NCA ioncubated 0-72 hours in MHRW (*D. magna* medium).
(c-d) Concentration of dissolved metal ion species released by 50 mg/L (c) NC and (d) NCA ioncubated 0-72 hours in minimal medium (*S. oneidensis* medium).
For these studies, a 10 mL aliquot was removed and subjected to ultra-centrifugation to remove suspended NCA and NC nanoparticles, after which the supernatant solution was analyzed by ICP-OES to determine the concentration of dissolved metal species released into the medium. Values reported as mean +/- S.D. (4 replicates from two independent experiment).

Metal ion release was compared for NC and NCA nanoparticles incubated in MHRW and minimal medium for 72 hours to determine the effects of Al doping and media composition on metal release, with results shown in Figure 4. In MHRW, NCA was characterized by reduced Ni and Co metal ion release compared to NC, and minimal detection of Al (Figure 4 a-b). Further, metal ion release was non-stoichiometric (incongruent) relative to bulk compositions for both NC and NCA nanoparticles in MHRW, which is consistent with previous results for lithium nickel manganese cobalt oxide (NMC) nanoparticles in MHRW.[36] In minimal medium (Figure 4 c-d), combined metal ion concentrations (Ni, Co, Al) were similar for both materials after 72 hours of incubation, indicating that the presence of Al did not reduce metal ion release to the same extent

as MHRW. Further, the stoichiometry of Ni, Co, and Al concentrations in minimal medium more closely reflected the bulk compositions (congruent release) for both NC and NCA, which contrasts with incongruent release in MHRW here and for previous studies investigating NMC nanomaterials.[27, 28, 34, 36, 62]

3.3 Computational modeling comparison of metal ion release for NC and NCA

Interpretation of the values of ΔG_T calculated using Equation 2 is carried out alongside other values. Specifically, we consider values of ΔG_T alongside values of μ_B (Eq. 3). We also tabulate the change in values of ΔG_T for a given metal between NCA and NC, defined as $\Delta(\Delta G_T)$. For $\Delta(\Delta G_T)$ values > 0, removing the M-OH group from NCA is less farovable relative to the same group removed from NC. Likewise, changes in μ_B are reported as $\Delta\mu_B$. Negative values for $\Delta\mu_B$ indicate NCA formulations have less unpaired electron density surrounding the vacancy site. We expect these materials to be most stable when anti-ferromagnetic couplings are maximized.[55]

Table 2: ΔG_T values (eV) and the total spin environment of neighboring metals (μ_B) comparing Ni removal after the sustitution of Al. Differences are given for ΔG_T and μ_B going from NC to NCA.

Structure	Site	ΔG_T (eV)	$\Delta(\Delta G_T)$ (eV)	μ_B	$\Delta\mu_B$
NC-NN-3	Ni^{6Ni}	-4.06	0.73	5.53	-2.73
NCA-NN-3	$Ni^{5Ni\text{-}1Al}$	-3.33		2.80	
NC-NN-1	$Ni^{5Ni\text{-}1Co}$	-3.75	0.21	4.56	-2.31
NCA-NN-1	$Ni^{4Ni\text{-}1Co\text{-}1Al}$	-3.54		2.25	
NC-nNN-1	$Ni^{5Ni\text{-}1Co}$	-4.21	0.98	4.67	-2.38
NCA-nNN-1	$Ni^{4Ni\text{-}1Co\text{-}1Al}$	-3.23		2.29	

Table 2 reports the values of ΔG_T (and other calculated values for comparison) for Ni-OH removals from supercells following the naming schemes described in Figures 1 and 2 and the accompanying text. For vacancy structures where Al is in the local environment of the removed metal (see Fig. 2, and sites in Table 2 with Al in the superscript), $\Delta(\Delta G_T) > 0$. This indicates that the Al doping reduces the tendency for Ni-OH release. This agrees with experimental observations for metal release in MHRW, where metal ion release was generally lower for NCA nanoparticles relative to NC. As disccussed in the Introduction, previous studies have shown the oxidation states play a key role in controlling ΔG_T.[32, 33] However, here we would not expect a

change in oxidation states as Ni is present as a 3+ cation in NC and Al is another 3+ cation. We test this assumption by comparing the electronic structure of Ni before and after Al substitution (**Figure S7**). No changes in the electronic structure were observed for Ni after the substitution of Al indicating the change in ΔG_T is not due to changes in oxidation states of the surface metals. Instead, we can correlate the changes in ΔG_T to the spin environment of the metals directly neighboring the site. Al^{3+} has a p^6 configuration where all electrons are paired, whereas Ni^{3+}, d^7, will have an unpaired electron in the e_g orbitals of the octahedral environment. By substituting Al in place of Ni, there are fewer unpaired electrons (and thus greater stability) surrounding the formed vacancy, as indicated by negative $\Delta\mu_B$ values. This agrees with previous work that observed Ni release was dependent on the spin environment when the oxidation state of Ni was held constant across different formulations.[55]

Values of ΔG_T between NC and NCA in Table 3 are also compared for cases where the vacancy site does not have a surface Al neighbor. For example, consider NC-NN $Co^{5Ni\text{-}1Co}$ (ΔG_T = -2.54 eV) and NCA-NN $Co^{5Ni\text{-}1Co}$ (ΔG_T = -2.46 eV). In this case, ΔG_T is more negative for a Co-OH removal from NC than in the analogous NCA, showing that the doped Al can impact metal release even when it is not occupying a lattice site local to the leaving group. In this example there is little to no change in the spin environment since the neighboring metals remain unchanged. A conclusion is that aluminum induces long-range stability in the lattice.

Table 3: ΔG_T values (eV) for Ni-OH or Co-OH removal from NC and NCA materials and total spin environments (μ_B). Also reported are values of $\Delta(\Delta G_T)$ (eV), which compares the energy of release for related NC and NCA materials in which the chemical environment is held constant. For $\Delta(\Delta G_T) > 0$, it is more favorable to release a M-OH group from the NC material relative to NCA. Values of $\Delta\mu_B$ denote the change in net spin between the NC and related NCA material.

Structure	Site	ΔG_T (eV)	$\Delta\Delta G_T$ (eV)	μ_B	$\Delta\mu_B$
NC-NN	Ni^{6Ni}	-4.06	0.44, 0.65	5.53	+0.09, +0.19
NCA-NN	Ni^{6Ni}	-3.41		5.62	
NCA-NN	Ni^{6Ni}	-3.62		5.72	
NC-nNN	$Ni^{4Ni\text{-}2Co}$	-3.54	0.21	3.42	+0.20
NCA-nNN	$Ni^{4Ni\text{-}2Co}$	-3.33		3.62	
NC-NN	$Ni^{3Ni\text{-}3Co}$	-4.21	0.03	2.26	-0.14
NCA-NN	$Ni^{3Ni\text{-}3Co}$	-4.18		2.12	
NC-nNN	Co^{6Ni}	-2.97	0.30	4.66	+0.09
NCA-nNN	Co^{6Ni}	-2.67		4.75	

NC-NN	$Co^{5Ni-1Co}$	-2.54	0.08	3.75	-0.02
NCA-NN	$Co^{5Ni-1Co}$	-2.46		3.73	

To further explore why it is thermodynamically less favorable to remove Ni or Co from NCA than NC, even when the leaving group does not have Al in the local coordination environment, we performed vibrational calculations and compare the energy values of the harmonic frequencies to assess bond rigidity in the NC versus NCA materials. When comparing the vibrational modes between NC and NCA, we see that all frequency values for NCA increase by 5-12 cm^{-1} (**Table S6**). This indicates that the bonding network must be stronger in NCA as a result of aluminum doping. The strengthened bonds, as supported by the vibrational analysis, are in line with the less favorable metal release reflected in the values of ΔG_T. Besides increasing the stability of the lattice, we can also measure the effect Al substitution will have on other properties of NCA as a cathode material by computing V_{int} and E_f as defined in Equations 4 and Ref 55 respectively. E_f values are reported per formula unit.

Table 4: Computed values for voltage and formation energies, before and after Al doping, for both NN and nNN configurations. Values of ΔV_{int} and ΔE_f denote the difference between the NC and NCA materials.

Composition (NC)	V_{int} (V)	E_f (eV)	Composition (NCA)	V_{int} (V)	E_f (eV)	ΔV_{int} (V)	ΔE_f (eV)
NC-NN-A	3.10	-63.03	NCA-NN-A	3.22	-66.68	+0.12	-3.65
NC-nNN-A	3.10	-63.04	NCA-nNN-A	3.21	-66.75	+0.11	-3.71

As a result of Al doping, the calculated values of V_{int} for modeled NCA increase by at least 0.11 V relative to NC. It has been observed in previous studies that the presence of Al will increase the voltage due to its lack of d-state electrons between oxygen and the Fermi energy.[55] This results in electrons requiring more energy to leave the system, causing the output voltage to increase. It is shown in Table 4 that the values of E_f are more favorable for the NCA material. The comparison of V_{int} and E_f values between NC and NCA, along with the vibrational analysis, all support the enhanced lattice stability resulting from doping Al into the NC material.

The final interpretation based on computational analysis considers how subsequent aqueous chemistry after the initial metal release may influence trends as a function of metal identity. Because the value of ΔG_3 for Co is 0.41 eV lower in energy than that of Ni (Table 1), the

relative values (reflected in $\Delta(\Delta G_T)$ in **Tables S3 & S4**) also decreases by that amount. This suggests that Ni-OH and Co-OH removal in the presence of lactate will be energetically on par and corroborates the experimental observation of more congruent metal release in minimal media. Likewise, the relatively large magnitude of ΔG_3 for Al leads to similar $\Delta G_T'$ values for Ni and Al, in line with observations that Ni and Al release similarly in the lactate-containing minimal media.

3.4 Biological impact of NCA and NC nanoparticles

In biological studies, we aimed to determine if Al substitution would affect acute toxicity towards two model freshwater organisms, *D. magna* (MHRW) and *S. oneidensis* (minimal medium). Figure 5a illustrates the percent survival for *D. magna* exposed to 0 - 100 mg/L NCA or NC nanoparticles after 48 hour exposure. *D. magna* survival was decreased compared to control after exposure to 50 and 100 mg/L NC nanoparticles, whereas NCA nanoparticles did not have a significant impact on survival for any of the nanoparticle doses measured. These results indicate that the chemical composition of NCA was more favorable to daphnid survival than NC. Previously, a nanoparticle-specific role for biological impact towards *D. magna* was reported for $LiNi_xMn_yCo_{1-x-y}O_2$ (NMC) nanomaterials, as Ni and Co ion concentrations released by the highest nanoparticle concentration tested (25 mg/L) did not reduce survival.[32, 36] Ni released by 50 and 100 mg/L NC was higher than concentrations previously reported for NMC in MHRW,[32, 36] and approached reported EC50 values for daphnid survival upon exposure to Ni ions.[68-72] The increased toxicity for NC compared to NCA could be due to the increased release of Ni ions into the media, although we cannot rule out other effects associated with direct interactions with daphnids (e.g., nanoparticle consumption).

Figure 5b illustrates relative viability for *S. oneidensis* exposed to 0 - 100 mg/L NCA or NC nanoparticles, as determined using a growth-based viability assay after 3 hour exposure.[63] NCA and NC nanoparticles each had a dose-dependent impact on *S. oneidensis* viability, which is consistent with previous results reported for NMC materials.[27, 34, 62] However, despite NC releasing higher concentrations of Ni and Co than NCA at the 3 hour time point, there were no significant differences in viability between NCA and NC nanoparticles for any of the doses measured here. These results suggest that metal ion release alone may not fully explain the

biological impact of NCA and NC towards *S. oneidensis*. Taken together, our results demonstrate that substitution of Al into the NC lattice reduced acute toxicity towards *D. magna*, while the biological impact towards *S. oneidensis* was similar for both materials. These combined results highlight challenges of redesign strategies aimed at reducing the biological impact of nanomaterials in the environment, where biological diversity and aqueous conditions can vary significantly.

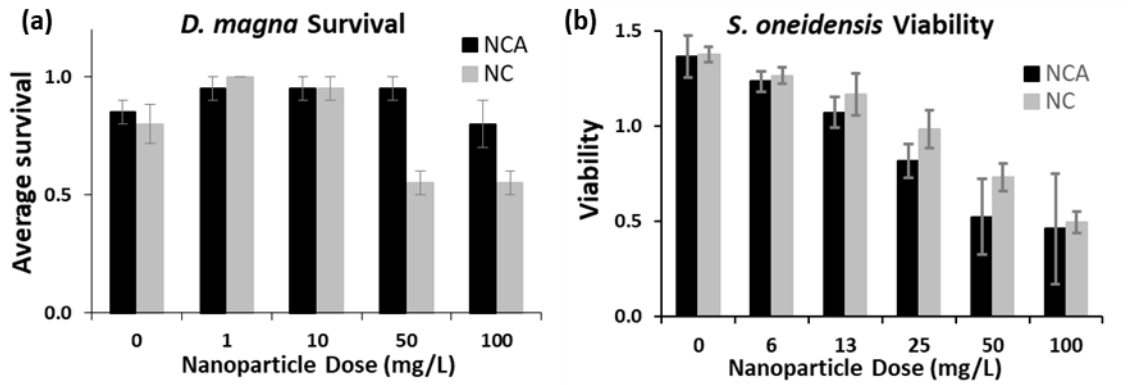

Figure 5: NC and NCA impact on (a) *D. magna* and (b) *S. oneidensis*. (a) Comparison of average survival for *D. magna* exposed to 0 – 100 mg/L NC (H = 15.529, df = 4, probability value = 0.004) or NCA (H = 5.111, df = 4, probability value = 0.276) nanoparticles. Statistical significance for daphnid survival after exposure to NC and NCA was assessed using the nonparametric Tukey test (degrees of freedom, df=4; n=4 replicate experiments; error bars represent standard error of the mean). (b) *S. oneidensis* viability was measured for 0 – 100 mg/L NCA or NC using a growth-based viability assay.[63]

4. Conclusions

NC and NCA were synthesized by a molten salt technique to determine how incorporation of Al into layered metal oxide materials influences metal release and toxicity towards model organisms under aqueous conditions. Metal ion concentrations released in minimal medium were nearly proportional to bulk composition (congruent release) for all nanomaterials after 72 hours of incubation, while the total metal ion release was substantially lower and did not correlate to bulk stoichiometry (incongruent release) in MHRW. Integrated experiment and theory demonstrate that the incorporation of Al reduces metal ion release in going from NC and NCA formulations under aqueous conditions in the absence of a strong chelating agent due to a decrease in the spin environment of the neighboring metals and results in a stronger bonding network. However, the presence of lactate in minimal medium enhances metal release from NC

and NCA compared to MHRW. We conclude this is due to energetically favorable chelation of lactate with the hydrated metal ion species. The relatively more favorable chelation with Co compared to Ni results in shifts in the release profiles from incongruent in MHRW to congruent in minimal medium. Finally, the biological impacts observed for two model organisms exposed to NC and NCA correlate with the release trends in their respective growth media. Together, our combined computational and experimental results provide chemical insights into how changes in nanoparticle composition and the presence of aqueous species in water influence metal release trends and subsequent biological impacts.

Author Contributions

Blake G. Hudson[a], Data curation, Formal Analysis, Writing-original draft, Writing-review & editing

Curtis M. Green[b], Data Curation, Formal Analysis, Validation, Writing-review & editing

Arun Kumar Pandiakumar[b], Conceptualization, Data Curation, Formal Analysis, Writing-original draft

Ali Abbaspour Tamijani[a], Data Curation, Writing-original draft

Natalie V. Hudson-Smith[c], Data curation, Formal Analysis, Investigation

Joseph T. Buchman[c], Data curation, Formal Analysis, Investigation

Meagan Koss[d], Data curation, Formal Analysis

Elizabeth D. Laudadio[b], Data curation, Formal Analysis

Michael P. Schwartz[b], Supervision, Formal Analysis, Writing – review & editing

Rebecca Klaper[d], Project administration, Supervision, Methodology, Resources, Writing – review & editing

Christy L. Haynes[b], Project administration, Supervision, Methodology, Resources, Writing – review & editing

Robert J. Hamers[b], Conceptualization, Project administration, Funding acquisition, Supervision, Methodology, Resources, Formal Analysis, Writing – review & editing

Sara E. Mason[a,e,*], Project administration, Supervision, Methodology, Resources, Writing – review & editing

Acknowledgements

This material is based upon work supported by the National Science Foundation under Grant No. CHE-2001611, the NSF Center for Sustainable Nanotechnology. The CSN is part of the Centers for Chemical Innovation Program. EDL and NVH acknowledge support from the National Science Foundation Graduate Research Fellowship Program. JTB was supported by the University of Minnesota Biotechnology Training Grant Program through the National Institutes of Health. The authors gratefully acknowledge use of facilities and instrumentation at the UW-Madison Wisconsin Centers for Nanoscale Technology (wcnt.wisc.edu) partially supported by the NSF through the University of Wisconsin Materials Research Science and Engineering Center (DMR-1720415). This research used Theory and Computation resources of the Center for Functional Nanomaterials (CFN), which is a U.S. Department of Energy Office of Science User Facility at Brookhaven National Laboratory under Contract No. DE-SC0012704.

REFERENCES:

1. G. E. Brown, V. E. Henrich, W. H. Casey, D. L. Clark, C. Eggleston, A. Felmy, D. W. Goodman, M. Grätzel, G. Maciel, M. I. McCarthy, K. H. Nealson, D. A. Sverjensky, M. F. Toney and J. M. Zachara, Metal Oxide Surfaces and Their Interactions with Aqueous Solutions and Microbial Organisms, *Chemical Reviews*, 1999, **99**, 77-174.
2. H. A. Al-Abadleh and V. H. Grassian, Oxide surfaces as environmental interfaces, *Surface Science Reports*, 2003, **52**, 63-161.
3. P. B. Kelemen and J. Matter, In situ carbonation of peridotite for CO2 storage, *Proceedings of the National Academy of Sciences*, 2008, **105**, 17295-17300.
4. A. Kappler and K. L. Straub, Geomicrobiological Cycling of Iron, *Reviews in Mineralogy and Geochemistry*, 2005, **59**, 85-108.
5. G. E. Brown and G. Calas, Environmental mineralogy – Understanding element behavior in ecosystems, *Comptes Rendus Geoscience*, 2011, **343**, 90-112.
6. S. M. Kraemer, A. Butler, P. Borer and J. Cervini-Silva, Siderophores and the Dissolution of Iron-Bearing Minerals in Marine Systems, *Reviews in Mineralogy and Geochemistry*, 2005, **59**, 53-84.
7. J. Baxter, Z. Bian, G. Chen, D. Danielson, M. S. Dresselhaus, A. G. Fedorov, T. S. Fisher, C. W. Jones, E. Maginn, U. Kortshagen, A. Manthiram, A. Nozik, D. R. Rolison, T. Sands, L. Shi, D. Sholl and Y. Wu, Nanoscale design to enable the revolution in renewable energy, *Energy Environ. Sci.*, 2009, **2**, 559-588.
8. S. Ghosh, M. A. Makeev, Z. Qi, H. Wang, N. N. Rajput, S. K. Martha and V. G. Pol, Rapid Upcycling of Waste Polyethylene Terephthalate to Energy Storing Disodium

Terephthalate Flowers with DFT Calculations, *ACS Sustainable Chemistry & Engineering*, 2020, **8**, 6252-6262.

9. J. A. Sulpizio, S. Ilani, P. Irvin and J. Levy, Nanoscale Phenomena in Oxide Heterostructures, *Annual Review of Materials Research*, 2014, **44**, 117-149.
10. P. Rozier and J. M. Tarascon, Review—Li-Rich Layered Oxide Cathodes for Next-Generation Li-Ion Batteries: Chances and Challenges, *J. Electrochem. Soc.*, 2015, **162**, A2490.
11. A. Chakraborty, S. Kunnikuruvan, S. Kumar, B. Markovsky, D. Aurbach, M. Dixit and D. T. Major, Layered Cathode Materials for Lithium-Ion Batteries: Review of Computational Studies on LiNi1–x–yCoxMnyO2 and LiNi1–x–yCoxAlyO2, *Chem. Mat.*, 2020, **32**, 915-952.
12. A. Du Pasquier, I. Plitz, S. Menocal and G. Amatucci, A comparative study of Li-ion battery, supercapacitor and nonaqueous asymmetric hybrid devices for automotive applications, *J. Power Sources*, 2003, **115**, 171-178.
13. K. Ozawa, Lithium-ion rechargeable batteries with $LiCoO_2$ and carbon electrodes: the $LiCoO_2$/C system, *Solid State Ionics*, 1994, **69**, 212-221.
14. K. Mizushima, P. C. Jones, P. J. Wiseman and J. B. Goodenough, Li_xCoO_2 ($0<x\leqslant1$): A new cathode material for batteries of high energy density, *Solid State Ionics*, 1981, **3**, 171-174.
15. K. Mizushima, P. C. Jones, P. J. Wiseman and J. B. Goodenough, Li_xCoO_2 ($0<x<-1$): A new cathode material for batteries of high energy density, *Mater. Res. Bull.*, 1980, **15**, 783-789.

16. W. Liu, P. Oh, X. Liu, M.-J. Lee, W. Cho, S. Chae, Y. Kim and J. Cho, Nickel-Rich Layered Lithium Transition-Metal Oxide for High-Energy Lithium-Ion Batteries, *Angewandte Chemie International Edition*, 2015, **54**, 4440-4457.

17. J. B. Goodenough and Y. Kim, Challenges for Rechargeable Li Batteries, *Chem. Mat.*, 2010, **22**, 587-603.

18. J. B. Goodenough and K.-S. Park, The Li-Ion Rechargeable Battery: A Perspective, *J. Am. Chem. Soc.*, 2013, **135**, 1167-1176.

19. M. G. S. R. Thomas, W. I. F. David, J. B. Goodenough and P. Groves, Synthesis and structural characterization of the normal spinel Li[Ni2]O4, *Mater. Res. Bull.*, 1985, **20**, 1137-1146.

20. J. R. Dahn, U. von Sacken, M. W. Juzkow and H. Al-Janaby, Rechargeable $LiNiO_2$ / Carbon Cells, *J. Electrochem. Soc.*, 1991, **138**, 2207-2211.

21. M. Broussely, F. Perton, J. Labat, R. J. Staniewicz and A. Romero, Li/LixNiO2 and Li/LixCoO2 rechargeable systems: comparative study and performance of practical cells, *J. Power Sources*, 1993, **43**, 209-216.

22. T. Ohzuku and A. Ueda, Why transition metal (di) oxides are the most attractive materials for batteries, *Solid State Ionics*, 1994, **69**, 201-211.

23. F. Zhang, X. a. Zhou, X. Fu, C. Wang, B. Wang, W. Liang, P. Wang, J. Huang and S. Li, Which is the winner between the single-crystalline and polycrystalline LiNi0.80Co0.15Al0.05O2 cathode in the lithium-ion battery?, *Materials Today Energy*, 2021, **22**, 100873.

24. M. Jo, M. Noh, P. Oh, Y. Kim and J. Cho, A New High Power LiNi0.81Co0.1Al0.09O2 Cathode Material for Lithium-Ion Batteries, *Advanced Energy Materials*, 2014, **4**, 1301583.

25. O. Velázquez-Martínez, J. Valio, A. Santasalo-Aarnio, M. Reuter and R. Serna-Guerrero, A critical review of lithium-ion battery recycling processes from a circular economy perspective, *Batteries*, 2019, **5**, 68.

26. D. H. P. Kang, M. Chen and O. A. Ogunseitan, Potential Environmental and Human Health Impacts of Rechargeable Lithium Batteries in Electronic Waste, *Environ. Sci. Technol.*, 2013, **47**, 5495-5503.

27. M. N. Hang, I. L. Gunsolus, H. Wayland, E. S. Melby, A. C. Mensch, K. R. Hurley, J. A. Pedersen, C. L. Haynes and R. J. Hamers, Impact of Nanoscale Lithium Nickel Manganese Cobalt Oxide (NMC) on the Bacterium Shewanella oneidensis MR-1, *Chem. Mat.*, 2016, **28**, 1092-1100.

28. J. W. Bennett, D. Jones, X. Huang, R. J. Hamers and S. E. Mason, Dissolution of Complex Metal Oxides from First-Principles and Thermodynamics: Cation Removal from the (001) Surface of Li(Ni1/3Mn1/3Co1/3)O-2, *Environ. Sci. Technol.*, 2018, **52**, 5792-5802.

29. J. Choi, E. Alvarez, T. A. Arunkumar and A. Manthiram, Proton Insertion into Oxide Cathodes during Chemical Delithiation, *Electrochemical and Solid-State Letters*, 2006, **9**, A241.

30. A. Manthiram and J. Choi, Chemical and structural instabilities of lithium ion battery cathodes, *J. Power Sources*, 2006, **159**, 249-253.

31. E. Billy, M. Joulié, R. Laucournet, A. Boulineau, E. De Vito and D. Meyer, Dissolution Mechanisms of LiNi1/3Mn1/3Co1/3O2 Positive Electrode Material from Lithium-Ion Batteries in Acid Solution, *ACS Appl. Mater. Interfaces*, 2018, **10**, 16424-16435.

32. J. T. T. Buchman, E. A. A. Bennett, C. Y. Wang, A. A. Tamijani, J. W. W. Bennett, B. G. G. Hudson, C. M. M. Green, P. L. L. Clement, B. Zhi, A. H. H. Henke, E. D. D. Laudadio, S. E. E. Mason, R. J. J. Hamers, R. D. D. Klaper and C. L. L. Haynes, Nickel enrichment of next-generation NMC nanomaterials alters material stability, causing unexpected dissolution behavior and observed toxicity to S. oneidensis MR-1 and D. magna, *Environ.-Sci. Nano*, 2020, **7**, 571-587.

33. J. W. Bennett, D. T. Jones, R. J. Hamers and S. E. Mason, First-Principles and Thermodynamics Study of Compositionally Tuned Complex Metal Oxides: Cation Release from the (001) Surface of Mn-Rich Lithium Nickel Manganese Cobalt Oxide, *Inorg. Chem.*, 2018, **57**, 13300-13311.

34. I. L. Gunsolus, M. Hang, N. Hudson-Smith, J. T. Buchman, J. Bennett, D. Conroy, S. E. Mason, R. Hamers and C. Haynes, Influence of nickel manganese cobalt oxide nanoparticle composition on toxicity toward Shewanella oneidensis MR-1: Redesigning for reduced biological impact, *Environmental Science: Nano*, 2017, **4**, 636-646.

35. C. H. Chen, J. Liu, M. E. Stoll, G. Henriksen, D. R. Vissers and K. Amine, Aluminum-doped lithium nickel cobalt oxide electrodes for high-power lithium-ion batteries, *J. Power Sources*, 2004, **128**, 278-285.

36. J. Bozich, M. Hang, R. Hamers and R. Klaper, Core chemistry influences the toxicity of multi-component metal oxide nanomaterials, lithium nickel manganese cobalt oxide and lithium cobalt oxide to Daphnia magna, *Environ. Toxicol. Chem.*, 2017, **36**, 2493-2502.

37. Y. Kim and D. Kim, Synthesis of High-Density Nickel Cobalt Aluminum Hydroxide by Continuous Coprecipitation Method, *ACS Appl. Mater. Interfaces*, 2012, **4**, 586-589.

38. S. Jouanneau and J. R. Dahn, Preparation, structure, and thermal stability of new NixCo1-2xMnx(OH)(2) (0 <= x <= 1/2) phases, *Chem. Mat.*, 2003, **15**, 495-499.

39. M. Guilmard, C. Pouillerie, L. Croguennec and C. Delmas, Structural and electrochemical properties of LiNi0.70Co0.15Al0.15O2, *Solid State Ionics*, 2003, **160**, 39-50.

40. H. Xie, K. Du, G. Hu, J. Duan, Z. Peng, Z. Zhang and Y. Cao, Synthesis of $LiNi_{0.8}Co_{0.15}Al_{0.05}O_2$ with 5-sulfosalicylic acid as a chelating agent and its electrochemical properties, *J. Mater. Chem. A*, 2015, **3**, 20236-20243.

41. J. K. Ngala, N. A. Chernova, M. Ma, M. Mamak, P. Y. Zavalij and M. S. Whittingham, The synthesis, characterization and electrochemical behavior of the layered $LiNi_{0.4}Mn_{0.4}Co_{0.2}O_2$ compound, *J. Mater. Chem.*, 2004, **14**, 214-220.

42. M. Okubo, E. Hosono, J. Kim, M. Enomoto, N. Kojima, T. Kudo, H. Zhou and I. Honma, Nanosize Effect on High-Rate Li-Ion Intercalation in $LiCoO_2$ Electrode, *J. Am. Chem. Soc.*, 2007, **129**, 7444-7452.

43. C. J. Powell and A. Jablonski, NIST Electron Inelastic-Mean-Free-Path Database, version 1.2 Standard Reference Database 71.*Journal*, 1999, DOI: http://dx.doi.org/10.18434/T48C78.

44. S. Tanuma, C. J. Powell and D. R. Penn, Calculation of electron inelastic mean free paths (IMFPs) VII. Reliability of the TPP-2M IMFP predictive equation, *Surf. Interface Anal.*, 2003, **35**, 268-275.

45. J. P. Perdew, K. Burke and M. Ernzerhof, Generalized gradient approximation made simple, *Phys. Rev. Lett.*, 1996, **77**, 3865-3868.

46. P. Giannozzi, O. Andreussi, T. Brumme, O. Bunau, M. Buongiorno Nardelli, M. Calandra, R. Car, C. Cavazzoni, D. Ceresoli, M. Cococcioni, N. Colonna, I. Carnimeo, A. Dal Corso, S. de Gironcoli, P. Delugas, R. A. DiStasio, A. Ferretti, A. Floris, G. Fratesi, G. Fugallo, R. Gebauer, U. Gerstmann, F. Giustino, T. Gorni, J. Jia, M. Kawamura, H. Y. Ko, A. Kokalj, E. Küçükbenli, M. Lazzeri, M. Marsili, N. Marzari, F. Mauri, N. L. Nguyen, H. V. Nguyen, A. Otero-de-la-Roza, L. Paulatto, S. Poncé, D. Rocca, R. Sabatini, B. Santra, M. Schlipf, A. P. Seitsonen, A. Smogunov, I. Timrov, T. Thonhauser, P. Umari, N. Vast, X. Wu and S. Baroni, Advanced capabilities for materials modelling with Quantum ESPRESSO, *Journal of Physics: Condensed Matter*, 2017, **29**, 465901.

47. P. Giannozzi, S. Baroni, N. Bonini, M. Calandra, R. Car, C. Cavazzoni, D. Ceresoli, G. L. Chiarotti, M. Cococcioni, I. Dabo, A. Dal Corso, S. de Gironcoli, S. Fabris, G. Fratesi, R. Gebauer, U. Gerstmann, C. Gougoussis, A. Kokalj, M. Lazzeri, L. Martin-Samos, N. Marzari, F. Mauri, R. Mazzarello, S. Paolini, A. Pasquarello, L. Paulatto, C. Sbraccia, S. Scandolo, G. Sclauzero, A. P. Seitsonen, A. Smogunov, P. Umari and R. M. Wentzcovitch, QUANTUM ESPRESSO: a modular and open-source software project for quantum simulations of materials, *J. Phys.-Condes. Matter*, 2009, **21**, 19.

48. K. F. Garrity, J. W. Bennett, K. M. Rabe and D. Vanderbilt, Pseudopotentials for high-throughput DFT calculations, *Comput. Mater. Sci.*, 2014, **81**, 446-452.

49. M. Hellenbrandt, The Inorganic Crystal Structure Database (ICSD) - Present and Future, *Crystallography Reviews*, 2004, **10**, 17-22.

50. H. J. Monkhorst and J. D. Pack, Special points for Brillouin-zone integrations, *Physical Review B*, 1976, **13**, 5188-5192.

51. A. Hirano, R. Kanno, Y. Kawamoto, Y. Takeda, K. Yamaura, M. Takano, K. Ohyama, M. Ohashi and Y. Yamaguchi, Relationship between non-stoichiometry and physical properties in LiNiO2, *Solid State Ionics*, 1995, **78**, 123-131.

52. A. Abbaspour Tamijani, J. W. Bennett, D. T. Jones, N. Cartagena-Gonzalez, Z. R. Jones, E. D. Laudadio, R. Hamers, J. A. Santana and S. E. Mason, DFT and Thermodynamics Calculations of Surface Cation Release in LiCoO2, *ChemRxiv*, 2019, DOI: 10.26434/chemrxiv.9764774.v1.

53. A. Togo and I. Tanaka, First principles phonon calculations in materials science, *Scr. Mater.*, 2015, **108**, 1-5.

54. X. Rong and A. M. Kolpak, Ab Initio Approach for Prediction of Oxide Surface Structure, Stoichiometry, and Electrocatalytic Activity in Aqueous Solution, *The Journal of Physical Chemistry Letters*, 2015, **6**, 1785-1789.

55. J. W. Bennett, D. T. Jones, B. G. Hudson, J. Melendez-Rivera, R. J. Hamers and S. E. Mason, Emerging investigator series: first-principles and thermodynamics comparison of compositionally-tuned delafossites: cation release from the (001) surface of complex metal oxides, *Environmental Science: Nano*, 2020, **7**, 1642-1651.

56. C. Ma, J. Borgatta, B. G. Hudson, A. A. Tamijani, R. De La Torre-Roche, N. Zuverza-Mena, Y. Shen, W. Elmer, B. Xing, S. E. Mason, R. J. Hamers and J. C. White, Advanced material modulation of nutritional and phytohormone status alleviates damage from soybean sudden death syndrome, *Nature Nanotechnology*, 2020, **15**, 1033-1042.

57. B. G. Hudson and S. E. Mason, Metal Release Mechanism and Electrochemical Properties of Lix(Ni1/3Mn1/3Co1/3)O2, *Applied Sciences*, 2022, **12**.

58. A. Urban, D.-H. Seo and G. Ceder, Computational understanding of Li-ion batteries, *npj Computational Materials*, 2016, **2**, 16002.

59. A. Jain, S. P. Ong, G. Hautier, W. Chen, W. D. Richards, S. Dacek, S. Cholia, D. Gunter, D. Skinner, G. Ceder and K. A. Persson, Commentary: The Materials Project: A materials genome approach to accelerating materials innovation, *APL Materials*, 2013, **1**, 011002.

60. K. E. Biesinger, L. R. Williams and W. H. van der Schalie, *Procedures for Conducting Daphnia magna Toxicity Bioassays*, U.S. Environmental Protection Agency, Office of Research and Development, Environmental Monitoring Systems Laboratory, 1987.

61. *OECD Guidelines for Testing Chemicals: Test No. 202: Daphnia sp., Acute Immobilisation Test*, Organisation for Economic Cooperation and Development, 2004.

62. M. N. Hang, N. V. Hudson-Smith, P. L. Clement, Y. Zhang, C. Wang, C. L. Haynes and R. J. Hamers, Influence of Nanoparticle Morphology on Ion Release and Biological Impact of Nickel Manganese Cobalt Oxide (NMC) Complex Oxide Nanomaterials, *ACS Appl. Nano Mater.*, 2018, **1**, 1721-1730.

63. T. A. Qiu, T. H. T. Nguyen, N. V. Hudson-Smith, P. L. Clement, D.-C. Forester, H. Frew, M. N. Hang, C. J. Murphy, R. J. Hamers, Z. V. Feng and C. L. Haynes, Growth-Based Bacterial Viability Assay for Interference-Free and High-Throughput Toxicity Screening of Nanomaterials, *Anal. Chem.*, 2017, **89**, 2057-2064.

64. J. H. Kim, S. T. Myung and Y. K. Sun, Molten salt synthesis of LiNi0.5Mn1.5O4 spinel for 5 V class cathode material of Li-ion secondary battery, *Electrochim. Acta*, 2004, **49**, 219-227.

65. D. Demirskyi, D. Agrawal and A. Ragulya, Neck formation between copper spherical particles under single-mode and multimode microwave sintering, *Mater. Sci. Eng. A-Struct. Mater. Prop. Microstruct. Process.*, 2010, **527**, 2142-2145.

66. T. Kimura, in *Advances in Ceramics - Synthesis and Characterization, Processing and Specific Applications*, ed. C. Sikalidis, InTech, Rijeka, 2011, DOI: 10.5772/20472, p. Ch. 04.

67. D. Qian, Y. Hinuma, H. Chen, L.-S. Du, K. J. Carroll, G. Ceder, C. P. Grey and Y. S. Meng, Electronic Spin Transition in Nanosize Stoichiometric Lithium Cobalt Oxide, *J. Am. Chem. Soc.*, 2012, **134**, 6096-6099.

68. B. G. Anderson, The apparent thresholds of toxicity to Daphnia magna for chlorides of various metals when added to Lake Erie water, *Transactions of the American Fisheries Society*, 1950, **78**, 96-113.

69. N. M. E. Deleebeeck, K. A. C. De Schamphelaere, D. G. Heijerick, B. T. A. Bossuyt and C. R. Janssen, The acute toxicity of nickel to Daphnia magna: Predictive capacity of bioavailability models in artificial and natural waters, *Ecotoxicology and Environmental Safety*, 2008, **70**, 67-78.

70. K. E. Biesinger and G. M. Christensen, Effects of Various Metals on Survival, Growth, Reproduction, and Metabolism of Daphnia magna, *Journal of the Fisheries Research Board of Canada*, 1972, **29**, 1691-1700.

71. E. F. Pane, C. Smith, J. C. McGeer and C. M. Wood, Mechanisms of Acute and Chronic Waterborne Nickel Toxicity in the Freshwater Cladoceran, Daphnia magna, *Environ. Sci. Technol.*, 2003, **37**, 4382-4389.

72. E. M. Traudt, J. F. Ranville and J. S. Meyer, Effect of age on acute toxicity of cadmium, copper, nickel, and zinc in individual-metal exposures to Daphnia magna neonates, *Environ. Toxicol. Chem.*, 2017, **36**, 113-119.